

Generalized free-space diffuse photon transport model based on the influence analysis of a camera lens diaphragm

Xueli Chen,^{1,2} Xinbo Gao,^{1,*} Xiaochao Qu,² Duofang Chen,² Xiaopeng Ma,² Jimin Liang,² and Jie Tian^{2,3}

¹Video and Image Processing System Laboratory, School of Electronic Engineering, Xidian University, Xi'an, Shaanxi 710071, China

²Life Sciences Research Center, School of Life Sciences and Technology, Xidian University, Xi'an, Shaanxi 710071, China

³Institute of Automation, Chinese Academy of Science, Beijing 100190, China

*Corresponding author: tian@ieee.org

Received 28 April 2010; revised 21 August 2010; accepted 11 September 2010; posted 13 September 2010 (Doc. ID 127716); published 7 October 2010

The camera lens diaphragm is an important component in a noncontact optical imaging system and has a crucial influence on the images registered on the CCD camera. However, this influence has not been taken into account in the existing free-space photon transport models. To model the photon transport process more accurately, a generalized free-space photon transport model is proposed. It combines Lambertian source theory with analysis of the influence of the camera lens diaphragm to simulate photon transport process in free space. In addition, the radiance theorem is also adopted to establish the energy relationship between the virtual detector and the CCD camera. The accuracy and feasibility of the proposed model is validated with a Monte-Carlo-based free-space photon transport model and physical phantom experiment. A comparison study with our previous hybrid radiosity-radiance theorem based model demonstrates the improvement performance and potential of the proposed model for simulating photon transport process in free space. © 2010 Optical Society of America

OCIS codes: 110.2970, 170.3880, 170.5280, 170.7050.

1. Introduction

Optical imaging has attracted much more attention in recent years due to its reasonable spatial and temporal resolution and affordable cost [1–4]. In particular, its noncontact measurement has become a valuable tool for the noninvasive detection because of its significant advantages in detection sensitivity, image quality, and system simplicity [5–8]. In noncontact optical imaging, the photon transport process can be divided into two parts—photon transport in tissues and in free space. Many numerical algorithms [9–11] have been proposed to simulate the

photon transport process in biological tissues with high efficiency and good applicability, but they cannot simulate photon transport process in free space. As a gold-standard algorithm, the Monte Carlo (MC) method can handle the photon transport process both in biological tissues and in free space [12,13]. However, it is time-consuming and needs a large number of photons to obtain an acceptable result. In addition, the method cannot be applied to the inverse process of photon transport in free space, which describes the reconstruction of light flux distribution on tissue surfaces from noncontact measurement on a CCD camera. Because of the complexity of the optical system and the Lambertian characteristics of the escaped photons, it is difficult to develop an

effective model for free-space diffuse photon transport in such a noncontact measurement.

To handle this problem, Ripoll *et al.* successfully proposed an effective free-space photon transport model that first demonstrated the possibility of realizing qualitative noncontact optical imaging [14]. However, this model is limited to modeling the image aberrations, perspective, and depth-of-field effects. Based on the proposed model, Schulz *et al.* put forward an improved and simplified model using the perspective projection method by replacing the camera lens with a virtual pinhole [15]. However, the improved model neglects the depth-of-field effects and can only apply to the case of a small aperture camera lens. In our previous study [16], a hybrid radiosity-radiance theorem (HRRT) based model has been proposed to simulate the photon transport process, which analyzed the influence of the camera lens and modeled it as a thin lens. The model reduced the influence of image aberrations, perspective, and depth-of-field effects by using the virtual detector, camera lens simplification model, radiance theorem, and the improvement of visibility factor. However, this model can only apply to the case of the large aperture camera lens effectively because it does not consider the influence of the camera lens diaphragm, which is also neglected in the existing models presented in Refs. [14,15]. The camera lens diaphragm is an inevitable component of the camera lens and plays an important role in a noncontact optical imaging system. Image quality is affected greatly by the camera lens diaphragm, such as in image range, image definition, and image intensity. Thus, to accurately model the photon transport process in free space, analysis of the camera lens diaphragm is absolutely necessary and important.

In this paper, a generalized free-space photon transport model is developed based on the influence analysis of the camera lens diaphragm, which is an improved version of the previous HRRT model [16]. Similarly, a propagation formula derived from the Lambertian source theory is used to describe the energy transformation when a photon propagates in free space. In the model, the camera lens is modeled as a combination of a thin lens and a camera lens diaphragm. Thus, the radiance theorem based on the thin-lens model can also be utilized to depict the energy relationship between the virtual detector and the CCD camera. In addition, the introduction of the camera lens diaphragm can further improve the depth-of-field effects so that we can obtain more accurate simulation images. The performance of the proposed generalized model is validated with Monte-Carlo-based free-space photon transport (MC-FSPT) model and physical phantom experiment. A comparison study with the HRRT model presents the improvement performance of the proposed generalized model and demonstrates its feasibility and potential for simulating the photon transport process in free space.

2. Theory and Method

A. Lambertian Source Theory

According to the knowledge of infrared physics, diffuse photons would act as a new Lambertian source once they have escaped from the diffuse medium and registered at the medium surface [17]. It is well-acknowledged that the Lambertian source is a radiation source that irradiates to the surrounding space isotropically. Thus, the microunit power $dP(\mathbf{r}_d)$ of a detector at position \mathbf{r}_d of the differential area and orientation $d\mathbf{A}$ emitted from a medium surface point \mathbf{r} of differential area and orientation $d\mathbf{S}$, in direction \mathbf{s} within a solid angle $d\Omega$, is given by [14]

$$dP(\mathbf{r}_d) = \frac{1}{\pi} J_n(\mathbf{r})(\mathbf{n}_s \cdot \mathbf{s}) d\Omega dS, \quad (1)$$

where $J_n(\mathbf{r})$ is the surface flux density and is calculated by considering the mismatched boundary condition; \mathbf{n}_s is the unit normal vector of $d\mathbf{S}$ and dS is the corresponding area. Considering the definition of the solid angle $d\Omega = -(\mathbf{dA} \cdot \mathbf{s})/|\mathbf{r}_d - \mathbf{r}|^2$, where \mathbf{s} always points to \mathbf{r}_d and integrates Eq. (1) over all the medium surface points, we obtain the total power $P(\mathbf{r}_d)$ at \mathbf{r}_d as

$$P(\mathbf{r}_d) = \frac{1}{\pi} \int_S J_n(\mathbf{r}) \xi(\mathbf{r}, \mathbf{r}_d) \frac{\cos \theta_s \cos \theta_d}{|\mathbf{r}_d - \mathbf{r}|^2} dAdS, \quad (2)$$

where $\cos \theta_s = \mathbf{n}_s \cdot \mathbf{s}$ is the cosine dependence of Lambert's law; $\cos \theta_d = -(\mathbf{dA} \cdot \mathbf{s})/dA$ accounts for the detector orientation with respect to the direction \mathbf{s} ; dA is the area of the differential detector unit; and $\xi(\mathbf{r}, \mathbf{r}_d)$ is a visibility factor that discards surface points invisible from the differential detector. Equation (2) distinctively depicts the transport characteristic of diffuse photons in free space emitted from the Lambertian source as the case shown in Fig. 1.

B. Camera Lens Diaphragms in an Optical Imaging System

In the optics design of a camera lens, designers should be concerned not only with the relevant issues of Gaussian optics, such as the magnification ratio of the camera lens and the conjugate distribution of object image, but also other crucial issues on imaging, such as image range, image definition, and image intensity. An actual camera lens is not a simple combination of several lenses, but a system consisting of various optical components, including a lens system and several diaphragms [18]. They are important optical function elements in a camera lens. The lens system puts emphasis on the transformation of the light beam, and the diaphragms focus on the receiving constraint of the line of sight [19]. Analysis of the lens system has been introduced in a previous paper [16], so this contribution presents only the analysis of the camera lens diaphragm.

The diaphragm aims to restrict the light beam entered into the camera lens, that is, useful lines of sight

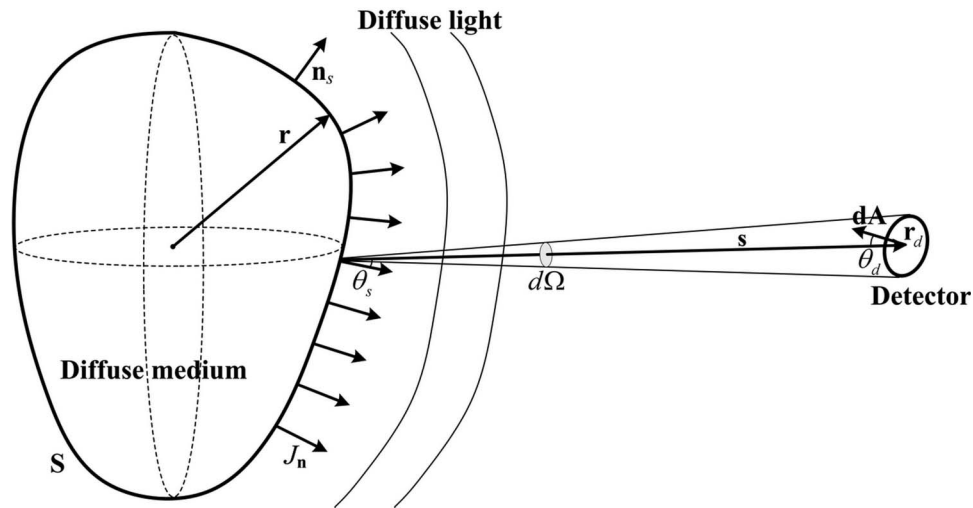


Fig. 1. Schematic diagram of the characteristic of diffuse photons transport in free space emitted from a Lambertian source.

are imaged in the camera lens and others are obstructed. Generally speaking, there are two basal types of diaphragms in any optical system: aperture diaphragm and field diaphragm [19,20]. The aperture diaphragm, also named “effective diaphragm,” is a crucial concept in the camera lens and is used to determine the size of the imaging beam, which varies with the size of aperture diaphragm and affects the luminance on the imaging plane. In an actual optical system, the size of the aperture diaphragm is adjusted by changing the aperture value, which satisfies the following equation:

$$D = \frac{F}{f_{\text{num}}}, \quad (3)$$

where D is the size of the aperture diaphragm called effective aperture in optics, as shown in Fig. 2; F is the focus of the camera lens; and f_{num} is the aperture value.

The function of the field diaphragm is to restrict the range of image. Image range can be limited by

various physical borders, such as the border of diaphragm, the border of lens, and the physical boundary of image sensor. These physical borders all work as the field diaphragm. Figure 2 presents two conventional positions of the diaphragm, at both sides of the lens system. In the case of Fig. 2(a), the diaphragm border acts as both the aperture diaphragm and the field diaphragm; in Fig. 2(b), the field diaphragm is performed by the border of the lens system [21]. Because the camera lens adopted in our optical imaging system is equipped with a diaphragm located at the back of the lens system, the following subsection just presents the influence analysis of the camera lens diaphragm shown in Fig. 2(b).

C. Modeling Camera Lens Diaphragm in a Simplified Optical Imaging System

According to the simplification theory of the imaging objective, the lens system adopted in an ideal optical system can be modeled as a thin-lens model [22,23]. However, this simplification considers only the Gaussian optics characteristic of the camera lens and neglects its physical factors, such as diaphragms.

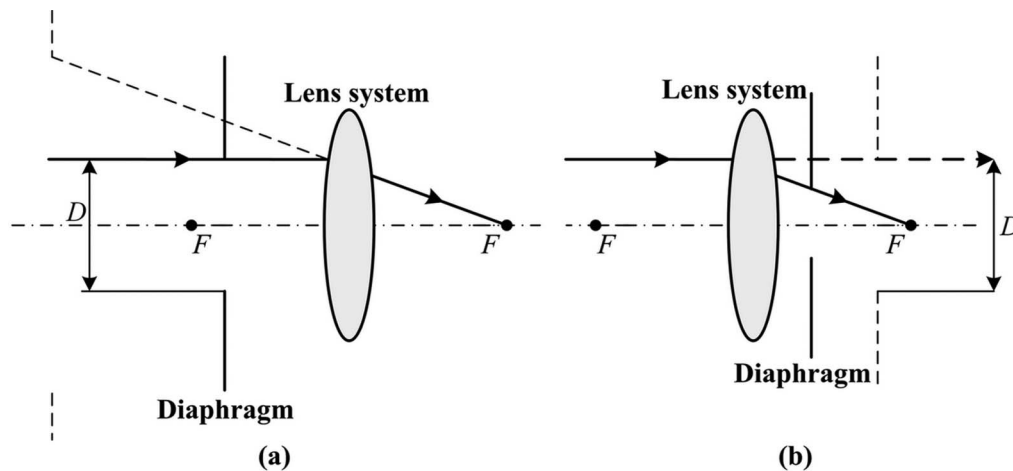


Fig. 2. Two types of diaphragms in any camera lens: (a) diaphragm located at the front of the lens system and (b) diaphragm located behind the lens system.

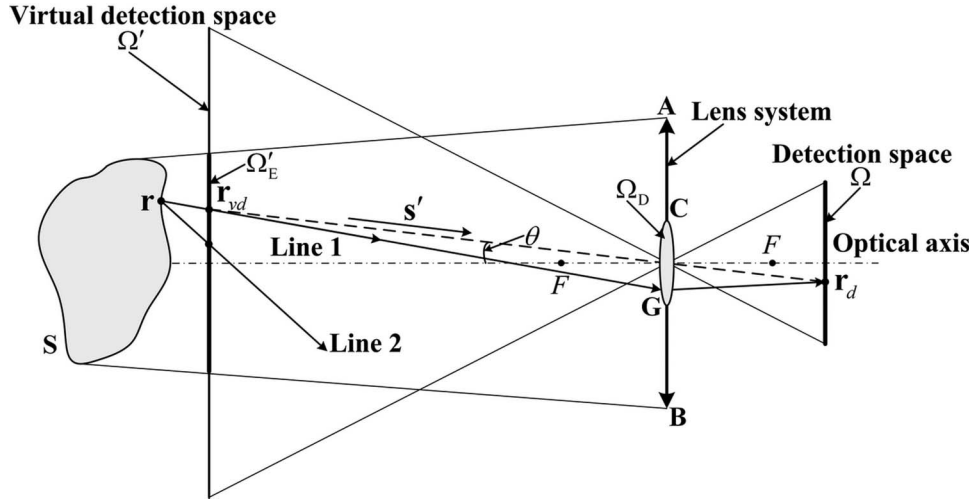


Fig. 3. Schematic diagram of modeling the camera lens diaphragm in the simplification of noncontact optical imaging system.

To accurately simulate the photon transport process in free space, we should take both influences into account in simplifying the camera lens. According to the aforementioned description of diaphragm, the camera lens adopted in the optical imaging system can be equivalently modeled as a simplified thin lens and a diaphragm. Therein, the diaphragm is virtual and located at the same position as the thin lens, as shown in Fig. 3, where AB shows the lens system and CG represents the virtual diaphragm.

In Fig. 3, the border of the lens system acts as the field diaphragm, and the virtual diaphragm as the aperture diaphragm. The lens system works to determine the range of image, and the virtual diaphragm is used to restrict the light beam entered into the camera lens. Assuming that S is the surface profile of the object and Ω' is the virtual detection space that is a focal space (a space constructed by the focal plane) of the detection space Ω , we can determine the effective virtual detection space Ω'_E by analyzing the relationship between the lens system and the surface profile, as shown in Fig. 3. Once the effective virtual detection space is obtained, we can further define a field visibility factor to restrict the range of image as

$$\alpha(\mathbf{r}, \mathbf{r}_{vd}) = \begin{cases} 1 & \text{If } (\mathbf{r}_{vd} \in \Omega'_E) \text{ AND } (\mathbf{s}_{\mathbf{r} \rightarrow \mathbf{r}_{vd}} \cap \mathbf{S} = \{\mathbf{r}\}), \\ 0 & \text{Otherwise,} \end{cases} \quad (4)$$

where $\alpha(\mathbf{r}, \mathbf{r}_{vd})$ is the field visibility factor, \mathbf{r} is a point on the surface profile and satisfies $\mathbf{r} \in \mathbf{S}, \mathbf{r}_{vd} \in \Omega'$ is a point at the virtual detection space and satisfies the lens law with the point \mathbf{r}_d at the detection space, Ω'_E is the effective virtual detection space and has the relationship of $\Omega'_E \subset \Omega'$, and $\mathbf{s}_{\mathbf{r} \rightarrow \mathbf{r}_{vd}}$ is the line of sight from \mathbf{r} to \mathbf{r}_{vd} .

The virtual diaphragm performs the function of aperture diaphragm and forms an effective aperture space Ω_D . Making use of Eq. (3), we can obtain the size of the effective aperture space. An effective

visibility factor can be introduced to determine the size of imaging beam as

$$\beta(\mathbf{r}, \mathbf{r}_d; \Omega_D) = \begin{cases} 1 & \text{If } \mathbf{s}_{\mathbf{r} \rightarrow \mathbf{r}_{vd}} \cap \Omega_D \neq \emptyset, \\ 0 & \text{If } \mathbf{s}_{\mathbf{r} \rightarrow \mathbf{r}_{vd}} \cap \Omega_D = \emptyset, \end{cases} \quad (5)$$

where $\beta(\mathbf{r}, \mathbf{r}_d; \Omega_D)$ is the effective visibility factor and Ω_D is the effective aperture space and has a circular area with a diameter D , calculated by Eq. (3). The expression $\mathbf{s}_{\mathbf{r} \rightarrow \mathbf{r}_{vd}} \cap \Omega_D \neq \emptyset$ can be interpreted that the line just passes through the effective aperture space, as Line 1, shown in Fig. 3; similarly, $\mathbf{s}_{\mathbf{r} \rightarrow \mathbf{r}_{vd}} \cap \Omega_D = \emptyset$ shows that the intersection point between the line and effective aperture space is out of the range of the effective aperture space, as Line 2, shown in Fig. 3.

D. Generalized Free-Space Diffuse Photon Transport Model and Numerical Implementation

Based on the derivation of the radiance theorem, the photon flux registered at the detector plane is equal to that at its conjugated virtual detector plane when an ideal optical imaging system is considered [16]. Thus, the corresponding relationship of energy between a detection point \mathbf{r}_d and a medium surface point \mathbf{r} can be expressed as

$$P(\mathbf{r}_d) = \frac{1}{\pi} \int_S J_n(\mathbf{r}) \xi(\mathbf{r}, \mathbf{r}_d) \frac{\cos \theta_s \cos \theta_d}{\left| \mathbf{r}_d - \mathbf{r} - \frac{l}{\cos \theta} \mathbf{s}' \right|^2} \frac{dA_d}{t^2} dS, \quad (6)$$

where $P(\mathbf{r}_d)$ is the total power of a differential detection area dA_d centered at \mathbf{r}_d ; l is the object image distance between the virtual detector plane and detector plane; \mathbf{s}' represents the direction from \mathbf{r}_{vd} to \mathbf{r}_d ; θ is the angle between the direction \mathbf{s}' and optical axis; θ_s is the angle between the differential medium surface normal and direction $\mathbf{s}_{\mathbf{r} \rightarrow \mathbf{r}_{vd}}$; θ_d is the angle between the normal of the virtual detector plane and direction $-\mathbf{s}_{\mathbf{r} \rightarrow \mathbf{r}_{vd}}$; t is the magnification ratio of the optical imaging system; and dA_d is a differential

detection area at the detector plane and satisfies $dA_d = t^2 dA_{vd}$, where dA_{vd} is a differential detection area at the virtual detector plane. Therein, the detection point \mathbf{r}_d and the virtual detection point \mathbf{r}_{vd} satisfy the following equation:

$$\mathbf{r}_d = \mathbf{r}_{vd} + \frac{l}{\cos\theta} \mathbf{s}'. \quad (7)$$

In Eq. (6), $\xi(\mathbf{r}, \mathbf{r}_d)$ is the visibility factor that takes into account the influence of the camera lens diaphragm presented in Eqs. (4) and (5). As a result, we obtain a generalized formula for diffuse photon transport in free space that takes into account the influence of the camera lens diaphragm as

$$P(\mathbf{r}_d) = \frac{1}{\pi} \int_S J_n(\mathbf{r}) T(\mathbf{r}, \mathbf{r}_d) dS, \quad (8)$$

where a function that accounts for diffuse photon transport in free space has been introduced:

$$T(\mathbf{r}, \mathbf{r}_d) = \alpha \left(\mathbf{r}, \mathbf{r}_d - \frac{l}{\cos\theta} \mathbf{s}' \right) \beta(\mathbf{r}, \mathbf{r}_d; \Omega_D) \times \frac{\cos\theta_s \cos\theta_d}{\left| \mathbf{r}_d - \mathbf{r} - \frac{l}{\cos\theta} \mathbf{s}' \right|^2} \frac{dA_d}{t^2}, \quad \mathbf{r} \in S. \quad (9)$$

The flux distribution at the detector plane can be obtained directly by the proposed model described in Eqs. (8) and (9). Compared with the published methods in Refs. [14–16], the proposed model concentrates more on modeling the camera lens, especially on the camera lens diaphragm. Furthermore, the proposed model will reduce to the pinhole model presented in Ref. [15] if the effective aperture is small enough to allow one line of sight to pass through for each surface point. If the effective aperture can be comparable to the size of the lens system, the proposed model would be performed as the thin-lens model presented in Ref. [16]. As a result, the proposed model is a generalized formula for the simulation of diffuse photon transport in free space.

3. Experiments and Results

In this section, three groups of verification experiments were designed and performed to evaluate the performance of the proposed model in this paper. First, numerical simulation and physical phantom experiments were conducted to validate the accuracy of the proposed model with a fixed aperture value. Then, a series of optical imaging experiments were carried out to illustrate the influence of camera lens diaphragm on image performance and show the effectiveness of the proposed model in the case of different aperture values. Finally, a comparison experiment with our previous HRRT model was conducted to demonstrate the improved performance of the proposed model.

In the optical imaging experiments, a nylon cylindrical homogeneous phantom of 15 mm radius and 30 mm height was designed and utilized. One small hole of 1 mm radius and 16 mm depth from the top surface of the phantom was drilled with a distance of 8 mm from the center to emplace a light source, as presented in Ref. [16]. The light source was made of luminescent solution that was extracted from a red luminescent light stick (Glow Products, Canada). Because the central wavelength of the luminescence light generated by the luminescent solution is about 650 nm, the optical properties of the phantom used the values measured at the wavelength of about 660 nm by a time-correlated single photon counting system [24]. The absorption coefficient is $\mu_a = 0.0138 \text{ mm}^{-1}$ and the reduced scattering coefficient is $\mu'_s = 0.91 \text{ mm}^{-1}$. After injecting the light source, the free volume of the small hole was filled with the same material solid stick to avoid leakage of light, and then the phantom was mounted on a 360° rotation stage. By rotating the phantom three 90°, luminescence light was registered by a liquid-water-cooled backilluminated CCD camera (Princeton Instruments/Acton, 2048B) coupled with a Nikkor Micro 55 mm $f/2.8$ camera lens.

In order to evaluate the performance of the proposed model, the mean error (ME) and correlation factor (CF) are introduced as presented in [16,25]

$$\bar{e} = \sum_{i=1}^N |P^{cal(i)} - P^{std(i)}| / N, \\ \rho = \sum_{i=1}^N (P^{cal(i)} - \bar{P}^{cal})(P^{std(i)} - \bar{P}^{std}) \times / ((N-1)\sigma(P^{cal})\sigma(P^{std})),$$

where \bar{e} and ρ are the value of the mean error and the correlation factor, respectively; the superscript *cal* represents the flux at the detector plane calculated by the proposed model, and *std* shows the flux obtained by the standard methods that are used to evaluate the performance of the proposed model; \bar{P} and σ are the mean value and the standard deviation of the flux distribution at the detector plane that can be either P^{cat} or P^{std} ; N is the total sample number at the detector plane; and $P^{(i)}$ is the power of the i th sample. The CF indicates the degree of correlation between the calculated and the standard flux, while the ME describes the discrepancy of them. Accordingly, the closer the CF gets to unity and the closer the ME gets to zero, the better the performance of the proposed model.

A. Experiment Verifications

In the experiment verifications, the MC-FSPT model and the real experiment were used as the standard methods to validate the accuracy of the proposed model. Results of the MC-FSPT model were obtained by the platform of Molecular Optical Simulation Environment (MOSE), which is an MC-based

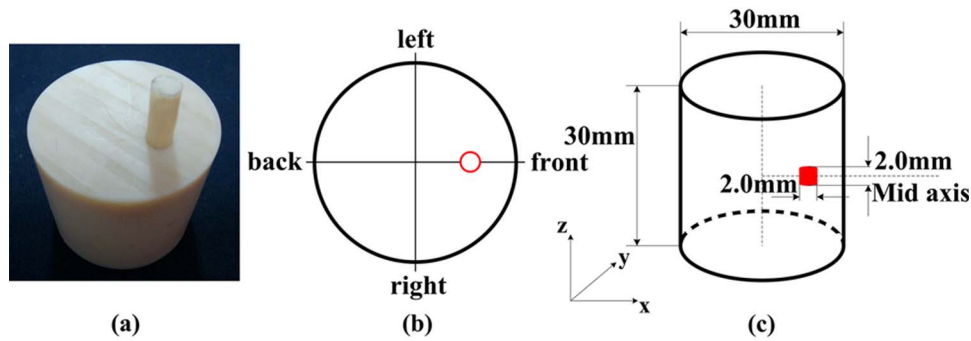


Fig. 4. (Color online) Experimental setup for comparison experiment showing (a) the physical phantom used in the optical imaging experiment, (b) four perspectives for the CCD camera to register escaped photons, (c) the numerical phantom used in the simulation and calculation.

simulation platform [26,27] and can be accessed freely on the website: <http://www.mosetm.net/>. Results of the real experiment were measured by the aforementioned noncontact optical imaging system with a fixed aperture value of $f_{\text{num}} = 8$.

The experimental setup is shown in Fig. 4. Therein, Fig. 4(a) presents the physical phantom used in the optical imaging experiment; Fig. 4(b) describes four perspectives for the CCD camera to register the outgoing luminescence light, including the front, left, back, and right perspective; and Fig. 4(c) shows the numerical phantom utilized in the calculation framework of the proposed model and the MC-FSPT model. In the calculation framework of the proposed model, the surface flux distribution J_n was obtained by MOSE after considering a mismatched boundary condition and then interpolated linearly between all the adjacent points to obtain a refined flux distribution. Once the refined surface flux distribution was obtained, we used the proposed model to calculate the flux distribution at the detector plane. For the MC-FSPT model, a one hundred million photon simulation was performed, which was 100 times as many as that used in determining the surface flux distribution for the calculation of the proposed model.

In view of the fact that the photon flux registered in the right perspective has the same trends in distribution as that in the left perspective, flux distributions of the front, left, and back perspective were examined in this subsection. All the flux was normalized to the maximum value versus the detection positions. Figure 5 shows the comparison results for the detector at z position: $z_d = 0.0, 2.0,$ and 4.0 mm. Therein, Figs. 5(a)–5(c) present the comparison results between the calculated flux of the proposed model and the simulated flux of the MC-FSPT model. Figures 5(d)–5(f) show comparisons between the calculated flux of the proposed model and the measured flux of the real experiment. In Fig. 5, the solid lines show the standard flux from the MC-FSPT model or real experiment, and the asterisks represent the calculated results of the proposed model. Furthermore, the ME and CF of the three perspectives were also calculated and listed in Table 1. Similar tendency and good agreement were observed in the cases ex-

amined, with average ME and CF being about 0.0219 and 0.9698. From Figs. 5(c) and 5(f), we find that the calculated flux of the proposed model seems a bit sparse, which was intrinsically caused by the inadequate spatial resolution of the refined surface flux. However, compared with the simulated flux of the MC-FSPT model, the sparsity of the calculated flux was a little better, which can also be seen from the ME and CF listed in Table 1. The comparison results indicated that the proposed model worked well in simulating the photon transport process in free space and appeared in good agreement with both the MC-FSPT model and the real experiment.

B. Influence of the Camera Lens Diaphragm on Image Quality

To illustrate the influence of the camera lens diaphragm on images registered at the CCD camera and the capability of the proposed model to simulate that influence, a group of experiments with different aperture values were conducted using the aforementioned noncontact optical imaging system. The experimental setup employed in the experiments was the same as that described in Subsection 3.A, except that the light source was a bit larger—about 6 mm in length. It should be noted that images registered on the CCD camera were captured under the same conditions, except for the aperture value. Left-perspective images on the CCD camera captured under different aperture values were observed, and four of them are presented in Figs. 6(a)–6(d). Using the proposed model, the corresponding calculated results are shown in Figs. 6(e)–6(h). As presented in Fig. 6(h), there was a little sparse in the calculated results when the aperture value was bigger than a certain value (about $f_{\text{num}} = 16$ in this experiment), which was probably caused by the inadequate spatial resolution of the refined surface flux distribution. Particularly, the degree of sparse for the results deepened with the increase of the aperture value under the condition of using the same surface flux distribution. If the spatial resolution of the surface flux distribution were adequately refined with the increase of aperture value, the sparse of the results would be improved. Nevertheless, compared with the

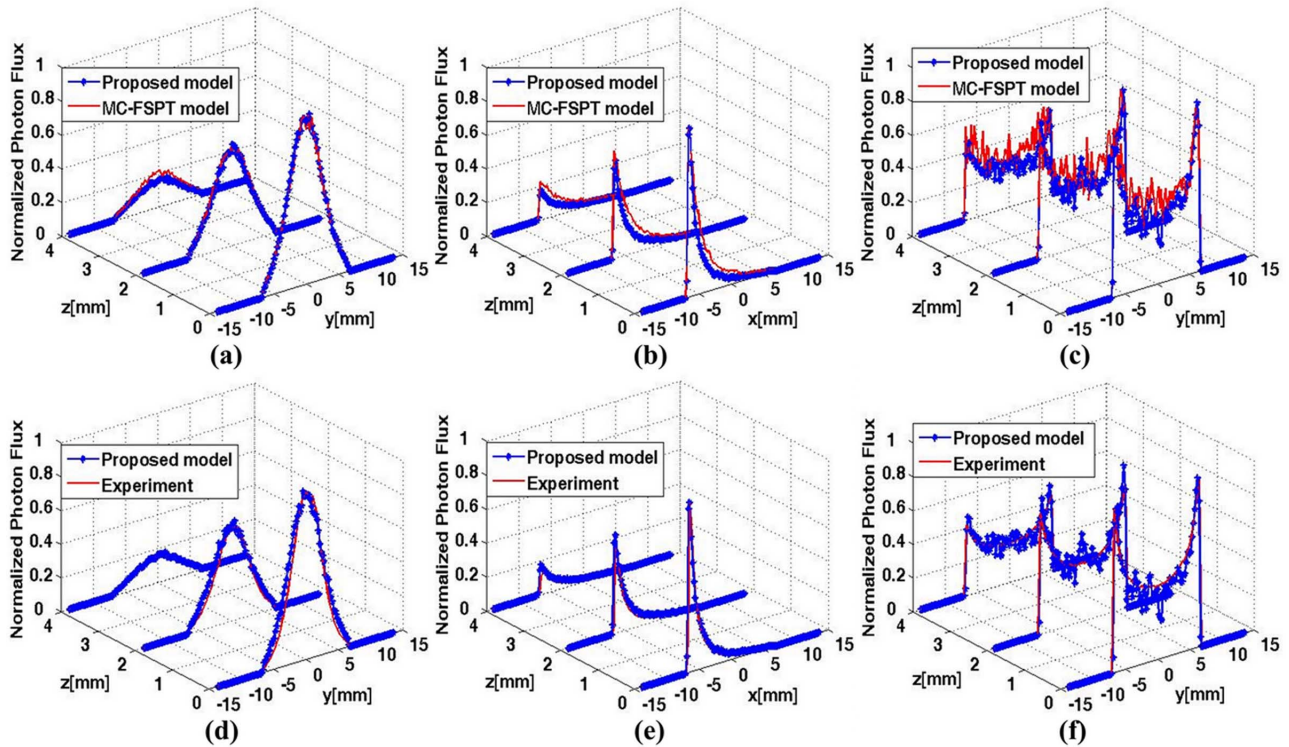


Fig. 5. (Color online) Comparison results between the calculated (asterisk lines) and standard flux (solid lines) at the detection position: $z_d = 0.0, 2.0,$ and 4.0 mm. (a)–(c) Comparison of flux between the proposed model and the MC-FSPT model; (d)–(f) comparison of flux between the proposed model and the real experiment. (a) and (d) front perspective, (b) and (e) left perspective, (c) and (f) back perspective.

experimental results, similar tendency and comparable distribution were addressed in all cases examined.

From Fig. 6 and no presented results, we find that two phenomena happen as the aperture value increases or as the size of the aperture diaphragm decreases in both the captured and the calculated images. First, the intensity becomes weaker and the definition gets worse. Because the function of the aperture diaphragm is to determine the size of the imaging beam, a smaller aperture diaphragm will lead to less light entered into the camera lens and imaged at the CCD camera. As a result, the intensity and signal-to-noise ratio of the image will decrease. Figure 7 presents a downtrend of the intensity as the aperture value increases. Figure 7(a) shows the downtrend of peak intensity, and Fig. 7(b) is the average intensity. Therein, the square lines represent the experimental

data and the asterisks show the calculated results. From Fig. 7, we determine that both the peak and the average intensity become smaller as the aperture value increases and the proposed model well-simulated the changes with extremely small discrepancies. The ME for the peak intensity comparison was 0.0166, and the normalized ME for the average intensity comparison was 0.0097. Furthermore, a relative quantitative relationship between the intensity and the aperture value was also observed where the intensity will decrease by almost half once the aperture value increases a scale, particularly as shown in Fig. 7(b).

Second, the distributional pattern of each image is different. To illustrate this difference, a distance from the position of the peak intensity point to the image border of the research object was used, as described in Fig. 8(a). By increasing the aperture value, the distance was gradually reduced.

Table 1. Error Comparison between the Calculated and the Standard Flux^a

Proposed Model Comparison	ME			CF		
	Front	Left	Back	Front	Left	Back
MC-FSPT model	0.0104	0.0179	0.0468	0.9968	0.9844	0.9606
Real experiment	0.0176	0.0113	0.0271	0.9917	0.9141	0.9711

^aThe second row presents the comparison of flux between the proposed model and the Monte Carlo method based on the free-space photon transport model; the third row shows the comparison between the proposed model and the real experiment. ME is defined as the mean error between the two compared objects; CF is the correlation factor of the two compared objects. The symbols *front*, *left*, and *back* represent the three different perspectives.

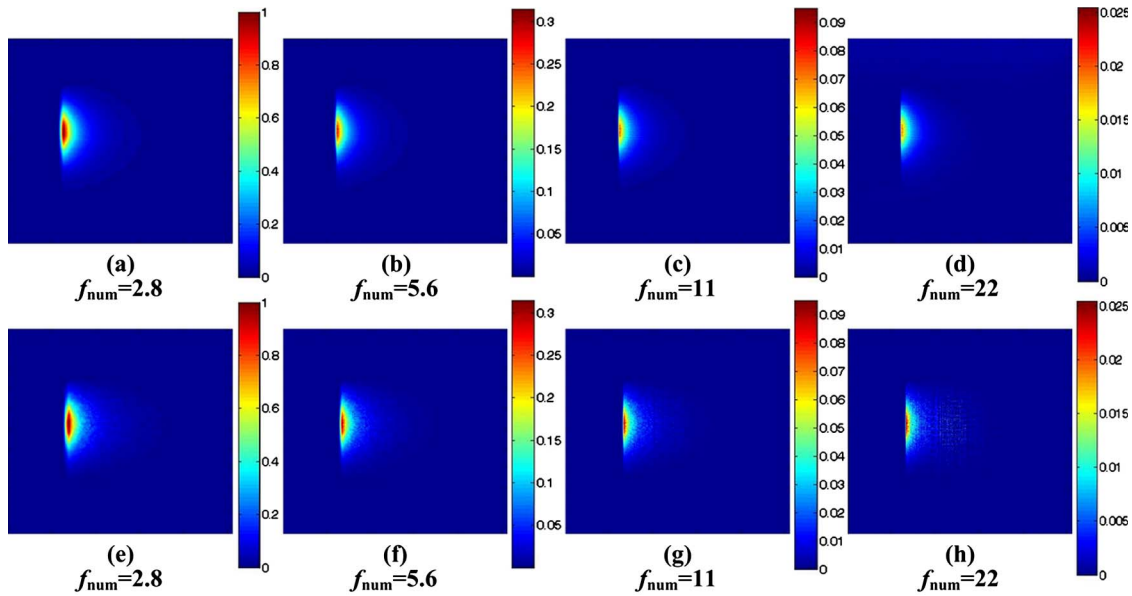


Fig. 6. (Color online) Comparisons between the calculated results of the proposed model (bottom row) and the experimental images on the CCD camera captured with different aperture values (top row) in the left perspective. (a)–(d) captured images at the CCD camera; (e)–(h) calculated results of the proposed model. For (a) and (e), $f_{\text{num}} = 2.8$; (b) and (f), $f_{\text{num}} = 5.6$; (c) and (g), $f_{\text{num}} = 11$; (d) and (h), $f_{\text{num}} = 22$.

Figure 8(b) presents the trend of the distance variation as the aperture value increases. Although there was a little difference between the calculated and the experimental results, the downtrend of them was consistent, with an average distance of 0.625 pixels.

As a result, we conclude that the performance of images registered at the CCD camera was factually affected by the camera lens diaphragm, such as image intensity and definition, image range, and intensity distribution. The comparisons between the calculated and the experimental results demonstrated that the proposed model can well-simulate the influence of the camera lens diaphragm. If a small aperture diaphragm is used in the imaging experiment and a larger aperture diaphragm or no aperture diaphragm is adopted in the calculation, an image of bad boundary will be obtained.

C. Improved Performance Demonstration

According to the aforementioned illustration of the influence of camera lens diaphragm on image performance, we infer that the HRRT model presented in our previous study [16] would work poorly when a small aperture diaphragm is used in the experiments. However, the proposed model in this paper overcomes this problem because of the consideration of the camera lens diaphragm. A comparison experiment was conducted in this subsection to present the improved performance of the proposed model compared with the HRRT one. The experimental setup is also presented in Fig. 4, and the experimental conditions are identical. In the comparison experiment, the surface flux distributions utilized in the two models were both obtained by MOSE and then interpolated linearly to approach a refined surface flux distribution.

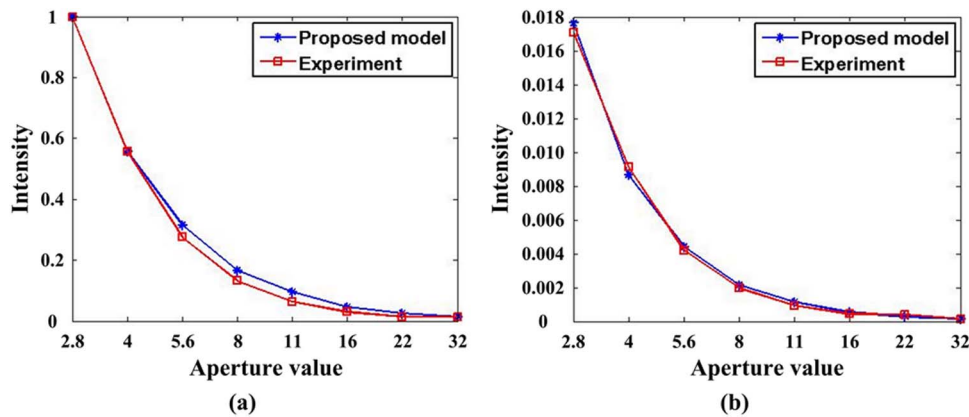


Fig. 7. (Color online) Corresponding relationship between the intensity variation and the different aperture values for both the calculated results (asterisk lines) and the experimental data (square lines). (a) Curve for variation of the peak intensity with the different aperture values. (b) Curve for variation of the average intensity with the different aperture values.

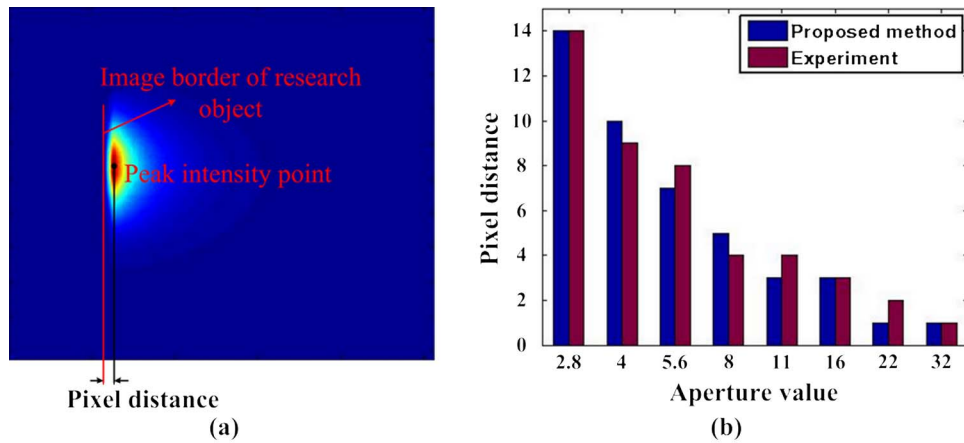


Fig. 8. (Color online) Corresponding relationship between the pixel distance and the different aperture values for both the calculated results (first column) and the experimental data (second column). (a) Schematic diagram of the definition of pixel distance. (b) Curve for variation of the pixel distance with the different aperture values.

Figure 9 presents the comparison images between the two models and the real experiment. The experimental result is shown in Fig. 9(a), and the corresponding calculated results obtained by the HRRT model and the proposed model are presented in Figs. 9(b) and 9(c). Moreover, the factors of the ME and CF were also calculated and listed in Table 2. From Fig. 9 and Table 2, we find that the proposed model performed better than the HRRT model in handling the boundary aberrations of the imaging region, which was intrinsically caused by no consideration of the camera lens diaphragm in the HRRT model. If the HRRT model is considered from the aspect of the camera lens diaphragm, it can be viewed as a model with an effective aperture equaling the size of the camera lens. Thus, the equivalent effective aperture will be much larger than the real one used in the experiment. Therefore, the HRRT result presented in Fig. 9(b) is comprehensible, according to the aforementioned illustration of the influence of the camera lens diaphragm. On the other hand, the improved performance for the front-perspective images is not significant, which can be seen from the values of the ME listed in Table 1 of this contribution and Table 2 of the previous study [16]. For the front per-

spective, the outgoing luminescence light registered at the detector plane is mainly gathered at the center of imaging region so that the intensity at the surrounding boundary area is extremely low. Thus, we conclude that the proposed model exhibited a well-improved performance on the boundary aberrations in the modeling photon transport process in free space. In conclusion, the proposed model greatly improved the simulation images on image range and flux distribution and provided much accurate simulated detection results for the simulation of optical imaging experiments.

4. Discussion and Conclusion

In this paper, a generalized free-space diffuse photon transport model was developed for the noncontact detection measurement. Similar to our previous study [16], this model also employed the hybrid radiosity-radiance theorem to depict the energy transformation for photon transports in a noncontact detection system. Furthermore, the influence analysis of the camera lens diaphragm was incorporated into the simplification model of the camera lens, which made the model suitable for processing image aberrations and depth-of-field effects. Compared with the existing

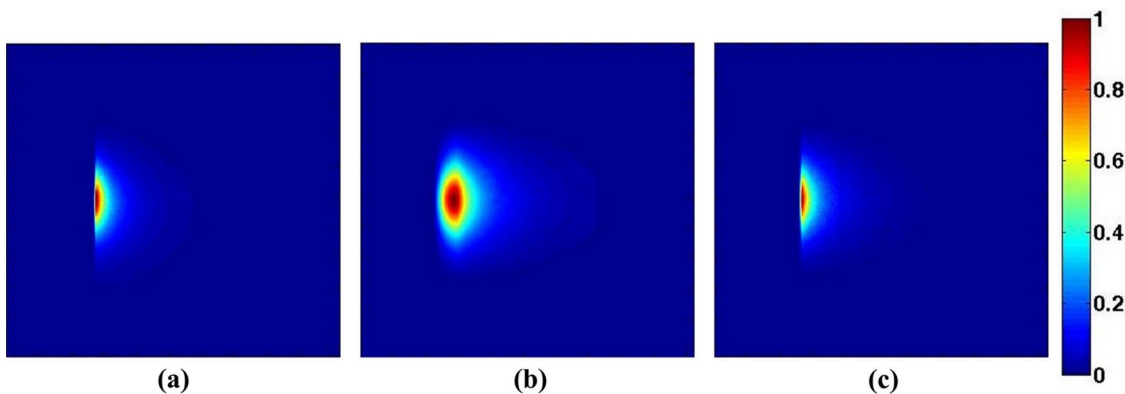


Fig. 9. (Color online) Comparisons of flux distribution at the detector plane between the calculation models and the real experiment: (a) experimental results, (b) calculations of the HRRT model, (c) calculations of the proposed mode.

Table 2. Error Comparison of the Proposed Model and the HRRT Model with the Real Experiment^a

Experimental Comparison	ME	CF
HRRT model	0.0421	0.8685
Proposed model	0.0110	0.9153

^aThe second row presents the comparison of flux between the HRRT model and the real experiment; the third row shows the comparison between the proposed model and the real experiment. ME is defined as the mean error between the two compared objects; CF is the correlation factor of the two compared objects.

models, the proposed model has the following features.

First, simplified model of the camera lens diaphragm is applied to describe the photon transport process in free space for the first time, to the best of our knowledge, which has a great influence on images registered at the CCD camera, such as the image range, image definition, and image intensity, and especially the quality of the image boundary. The proposed generalized model can be better used to handle the boundary aberrations of the image region than the existing models. In addition, the introduction of virtual detector plane and radiance theorem contributes to eliminate the perspective effects. Therefore, simulated images are more comparable to the images captured by the CCD camera.

Second, the proposed model is a generalized formula for simulating the photon transport process in free space, which contains two extreme cases, that is, a pinhole lens based model [15] and a thin-lens based model [16]. If the effective aperture is so small that only one line of sight can pass through for each surface point, the model is reduced to the pinhole lens based model. Otherwise, if the effective aperture is comparable to the size of the lens system, the model would be performed as the thin-lens based model. Furthermore, the depth-of-field effects of the optical imaging system are relevant to the effective aperture, which is determined by the size of the aperture diaphragm. Thus, the proposed generalized model can be better to process the problem of depth of field.

On the other hand, the proposed generalized model is accurate to a great extent, but it is a little time-consuming. To achieve a smoother simulation result, we must interpolate the surface flux distribution to guarantee the adequately refined surface spatial resolution. As a result, it makes the computation much more time-consuming. Fortunately, with the development of technology, the parallel strategy and the graphics processing unit (GPU) technique can be adopted to speed up the proposed generalized model. And the corresponding work is ongoing. In addition, the proposed model is developed based on the assumption that the photons escaping from the medium surface are diffuse. If the surface light distribution is not diffuse but anisotropic, the resulting transport function from the medium surface to the CCD camera should be far more complicated because of the angle dependency.

In conclusion, we have presented a generalized free-space diffuse photon transport model based on the influence analysis of a camera lens diaphragm in this paper. Preliminary experimental results demonstrated the feasibility and potential of the proposed generalized model. Our future work will concentrate on the acceleration of the generalized model based on the GPU-based technique and modeling the far more complicated transport function. The corresponding results will be reported later.

This work is supported by the Program of the National Basic Research and Development Program of China (973 Program) under grants 2006CB705700 and 2011CB707702, the Chinese Academy of Sciences (CAS) Hundred Talents Program, the National Natural Science Foundation of China (NSFC) under grants 81090272, 81000632, 30900334, and 60771068, the Shaanxi Provincial Natural Science Foundation Research Project under grant 2009JQ8018, and the Fundamental Research Funds for the Central Universities.

References

1. B. W. Rice, M. D. Cable, and M. B. Nelson, "In vivo imaging of light-emitting probes," *J. Biomed. Opt.* **6**, 432–440 (2001).
2. R. Weissleder and V. Ntziachristos, "Shedding light onto live molecular targets," *Nat. Med.* **9**, 123–128 (2003).
3. V. Ntziachristos, J. Ripoll, L. V. Wang, and R. Weissleder, "Looking and listening to light: the evolution of whole-body photonic imaging," *Nat. Biotechnol.* **23**, 313–320 (2005).
4. J. Tian, J. Bai, X. Yan, S. Bao, Y. Li, W. Liang, and X. Yang, "Multimodality molecular imaging," *IEEE Eng. Med. Biol. Mag.* **27**, 48–57 (2008).
5. R. B. Schulz, J. Ripoll, and V. Ntziachristos, "Non-contact optical tomography of turbid media," *Opt. Lett.* **28**, 1701–1703 (2003).
6. N. Deliolanis, T. Lasser, D. Hyde, A. Soubert, J. Ripoll, and V. Ntziachristos, "Free-space fluorescence molecular tomography utilizing 360° geometry projections," *Opt. Lett.* **32**, 382–384 (2007).
7. R. B. Schultz, J. Peter, and W. Semmler, "Comparison of non-contact and fiber-based fluorescence-mediated tomography," *Opt. Lett.* **31**, 769–771 (2006).
8. H. Meyer, A. Garofalakis, G. Zacharakis, S. Psycharakis, C. Mamalaki, D. Kioussis, E. N. Economou, V. Ntziachristos, and J. Ripoll, "Noncontact optical imaging in mice with full angular coverage and automatic surface extraction," *Appl. Opt.* **46**, 3617–3627 (2007).
9. S. R. Arridge, "Optical tomography in medical imaging," *Inverse Probl.* **15**, R41–R93 (1999).
10. S. R. Arridge and J. C. Schotland, "Optical tomography: Forward and inverse problems," *Inverse Probl.* **25**, 123010 (2009).
11. R. Elaloufi, S. R. Arridge, R. Pierrat, and R. Carminati, "Light propagation in multilayered scattering media beyond the diffusive regime," *Appl. Opt.* **46**, 2528–2539 (2007).
12. L. V. Wang, S. L. Jacques, and L. Q. Zheng, "MCML-Monte Carlo modeling of photon transport in multi-layered tissues," *Comput. Methods Programs Biomed.* **47**, 131–146 (1995).
13. D. G. Fischer, S. A. Prahl, and D. D. Duncan, "Monte Carlo modeling of spatial coherence: free space diffraction," *J. Opt. Soc. Am. A* **25**, 2571–2581 (2008).
14. J. Ripoll, R. B. Schulz, and V. Ntziachristos, "Free-space propagation of diffuse light: theory and experiment," *Phys. Rev. Lett.* **91**, 103901 (2003).

15. R. B. Schulz, J. Peter, W. Semmler, C. D' Andrea, G. Valentini, and R. Cubeddu, "Quantifiability and image quality in non-contact fluorescence tomography," *Proc. SPIE* **5859**, 58590Z (2005).
16. X. Chen, X. Gao, X. Qu, J. Liang, L. Wang, D. Yang, A. Garofalakis, J. Ripoll, and J. Tian, "A study of photon propagation in free-space based on hybrid radiosity-radiance theorem," *Opt. Express* **17**, 16266–16280 (2009).
17. J. Ripoll and V. Ntziachristos, "Imaging scattering media from a distance: theory and applications of non-contact optical tomography," *Mod. Phys. Lett. B* **18**, 1403–1431 (2004).
18. C. Kolb, D. Mitchell, and P. Hanrahan, "A realistic camera model for computer graphics," in *Proceedings of the 22nd Annual Conference on Computer Graphics and Interactive Techniques* (ACM, 1995), pp. 317–324.
19. B. Du and J. Wang, *Electron Optics* (Tsinghua University, 2002).
20. Q. Tian, Y. Liao, and L. Sun, *Engineering Optics* (Tsinghua University, 2004).
21. Y. Zhang, *Applied Optics* (Publishing House of Electronics Industry, 2008).
22. M. Aggarwal and N. Ahuja, "A pupil-centric model of image formation," *Int. J. Comput. Vision* **48**, 195–214 (2002).
23. M. Aggarwal and N. Ahuja, "A new imaging model," in *Proceedings of the International Conference on Computer Vision* (IEEE, 2001), pp. 82–89.
24. D. Qin, H. Zhao, Y. Tanikawa, and F. Gao, "Experimental determination of optical properties in turbid medium by TCSPC technique," *Proc. SPIE* **6434**, 64342E (2007).
25. H. K. Kim and A. H. Hielscher, "A PDE-constrained SQP algorithm for optical tomography based on the frequency-domain equation of radiative transfer," *Inverse Probl.* **25**, 015010 (2009).
26. H. Li, J. Tian, F. Zhu, W. X. Cong, L. V. Wang, and G. Wang, "A Mouse Optical Simulation Environment (MOSE) to investigate bioluminescent phenomena in the living mouse with the Monte Carlo method," *Acad. Radiol.* **11**, 1029–1038 (2004).
27. N. Ren, J. Liang, X. Qu, J. Li, B. Lu, and J. Tian, "GPU-based Monte Carlo simulation for light propagation in complex heterogeneous tissues," *Opt. Express* **18**, 6811–6823 (2010).